

http://pubs.acs.org/journal/aelccp

Moisture-Stable Intermediate Phase Manipulation for Efficient Perovskite Solar Cells Fabricated in Ambient Air

Luyao Yan, Hao Huang, Peng Cui, Yingying Yang, Zhenhuang Su, Yi Lu, Min Wang, Zhineng Lan, Shujie Qu, Benyu Liu, Changxu Sun, Liang Li, Shuxian Du, Fu Yang, Xingyu Gao, and Meicheng Li*



Cite This: ACS Energy Lett. 2025, 10, 5156-5164



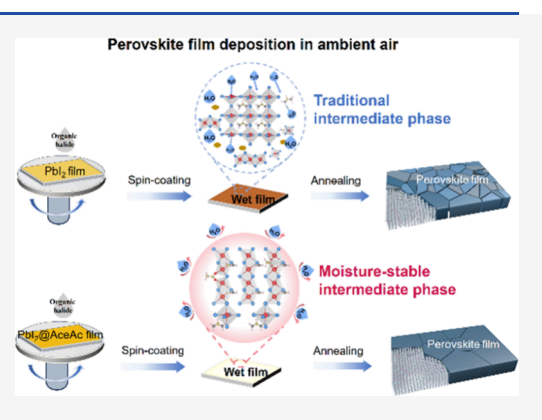
ACCESS

III Metrics & More

Article Recommendations

Supporting Information

ABSTRACT: Fabricating high-efficiency perovskite solar cells (PSCs) in ambient air can facilitate their low-cost industrialization. However, the metastable wet-film stage before annealing during the film deposition process is susceptible to moisture invasion, making it difficult to form blackphase formamidinium lead iodide (α -FAPbI $_3$) perovskites in ambient air. Herein, we construct a moisture-stable intermediate phase dominated by δ -FAPbI $_3$ in the metastable wet-film stage using acetimidamidal acetate (AceAc). AceAc can induce the formation of δ -FAPbI $_3$ to resist the invasion of moisture on a wet film, further transforming the formed δ -FAPbI $_3$ into pure α -FAPbI $_3$ in the presence of MACl. The resulting PSCs fabricated in ambient air achieve a power conversion efficiency (PCE) of 26.5% (certified at 25.9%) and maintain 98% of the initial PCE after 11000 h of aging under air conditions (25% relative humidity (RH) and 25 °C).



erovskite solar cells (PSCs) have undergone significant advances in recent years, but their stability remains a major challenge, limiting their practical application. Even during the preparation process, perovskite films can be affected by external factors such as moisture and oxygen. 1-4 Currently, the fabrication of most high-efficiency PSCs relies on an inert atmosphere or protected environment with extremely low humidity; this vital approach prevents disturbances during α -FAPbI $_3$ crystallization. Even in an inert atmosphere glovebox, various methods have been proposed to overcome the challenge that α -FAPbI₃ is not energetically favorable at room temperature, ensuring the attainment of high-quality perovskite films.⁵⁻⁷ However, maintaining the potential low-cost advantage of PSCs can promote their commercialization; thus, low-cost fabrication methods in unprotected ambient air need to be explored to develop high-efficiency PSCs.8-10

In ambient air, moisture inevitably damages the crystallization of FAPbI₃, easily leading to the formation of nonphotoactive phases and structural defects such as pinholes during FAPbI₃ film formation. ^{11,12} This mainly occurs because moisture disrupts the precursor solution balance before film formation and interferes with the nucleation and growth processes during film formation. ¹³ Extensive research has been conducted to mitigate the impact of moisture on perovskite crystallization and to produce high-efficiency PSCs in ambient air through various strategies, including thermal protection, ^{14,15} solvent engineering, ^{16,17} additive engineering, ^{18–21} and others. ^{22–24} Notably, an ionic liquid was proposed as a solvent to promote vertical growth of PbI₂, increasing the power conversion efficiency (PCE) of PSCs prepared in ambient air to 24.1%. ²⁵ Previously, we used guanabenz acetate salt to block the hydration of perovskite and further optimized the electron transport layer, achieving high-efficiency PSCs in ambient air. ^{26,27} Although many efforts have been made to improve the PCE of air-fabricated PSCs over 26%, understanding the crystallization mechanism, including phase evolution under ambient conditions, is essential, especially considering the intrinsic rapid crystallization kinetics of FAPbI₃ and external moisture invasion. This clarification can facilitate the achievement of scalable, reproducible, and high-quality films as well as the application of corresponding efficient PSCs.

Herein, we monitored the in situ crystallization process of FAPbI₃ films under humid conditions and demonstrated that

Received: August 4, 2025 Revised: September 3, 2025 Accepted: September 23, 2025



ACS Energy Letters http://pubs.acs.org/journal/aelccp Letter

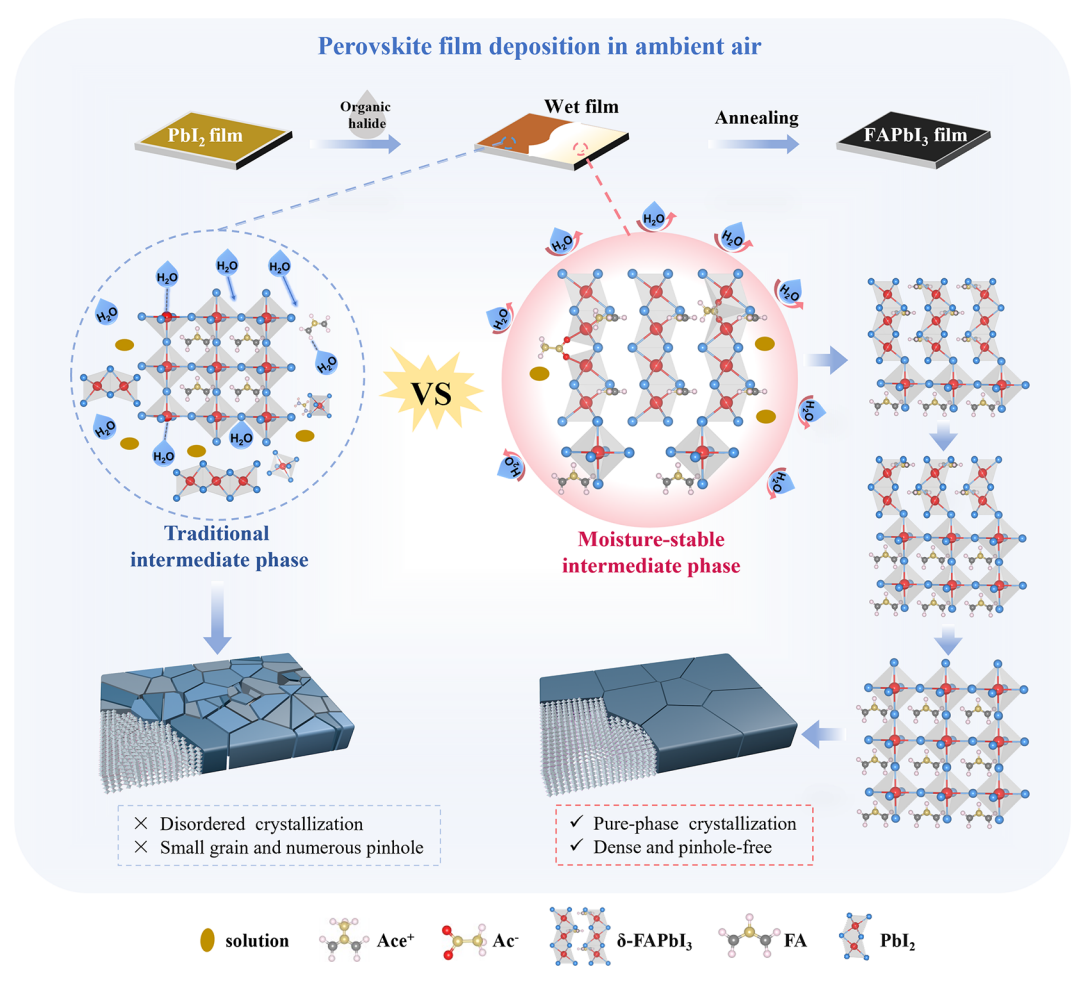


Figure 1. Diagram of perovskite crystallization in ambient air.

the destruction caused by moisture on the metastable wet films is the primary factor contributing to disordered crystallization (Supporting Information Figure S1 and Note S1). Inspired by the δ -FAPbI₃ that is more thermodynamically stable, we introduced acetamidinium acetate (AceAc, with its chemical structure shown in Figure S2) into the PbI₂ precursor to construct a moisture-stable intermediate phase dominated by δ -FAPbI₃ in the metastable wet film; its presence was confirmed by in situ grazing-incidence wide-angle X-ray scattering (GIWAXS). This moisture-stable intermediate phase with thermodynamic stability can protect the wet film from moisture invasion and then slowly and orderly transform into ideal α -FAPbI₃ through a purified phase transition in the presence of MACl, leading to a high-quality perovskite film fabricated in ambient air (Figure 1). The resulting PSCs fabricated in ambient air achieved a PCE of 26.5% (certified at 25.9% and 0.08 cm²). And, for the 1 cm² PSCs, a PCE of 25.3% was achieved (certified at 24.3%). Furthermore, based on the experiences of dozens of Chinese PSC companies and related literature, ²⁸⁻³¹ we calculated and compared the costs of building 100 MW production lines under atmospheric protection and ambient air conditions. Fabrication of these PSCs in ambient air can reduce equipment costs by 22 and 28% compared to the use of gloveboxes and ultralow-humidity clean rooms, respectively (Table S1). Thus, this method of manufacturing high-efficiency PSCs in ambient air could greatly facilitate the low-cost commercialization process of PSCs.

Cubic α -FAPbI₂ is one of the most promising materials for efficient PSCs, and its formation often occurs alongside a hexagonal δ -FAPbI₃ phase.^{6,32} Although δ -FAPbI₃ is nonphotoactive, it offers higher thermodynamic stability and is less sensitive to moisture than α -FAPbI₃, providing greater resistance to ambient moisture (Figure S3, Table S2, and Note S2). While methylamine (MA)-based additives effectively promote the formation of α -FAPbI₃, we explore using the Acebased additive to facilitate the formation of δ -FAPbI₃, given that Ace⁺ has a relatively larger molecular size (Table S3).^{33,34} After perovskite crystallization completes, residual Ace+ bonds to grain boundaries or surface sites to fill the FA+ vacancies without adversely affecting the crystal lattice. Pseudohalogen anions have been reported to induce the transformation of moisture-stable δ -FAPbI₃ to α -FAPbI₃ and regulate the perovskite crystallization. ^{35,36} Based on our previous study, we used Ac⁻ as the anion in conjunction with the Ace⁺-based salt.

We monitored the perovskite film formation process in ambient air using synchrotron-based in situ GIWAXS to explore the crystallization kinetics of the perovskite. As shown in Figure 2a,b, four stages occur during film formation. Stage I (0–30 s) and stage II (30–90 s) represent the spin-coating process of the PbI₂ precursor and the corresponding annealing process, respectively. Subsequently, when the organic-halide precursors are added dropwise to the PbI₂ film, stage III (90–120 s), corresponding to the wet-film stage, begins with an evident signal change. Stage IV (120–200 s) is the last stage

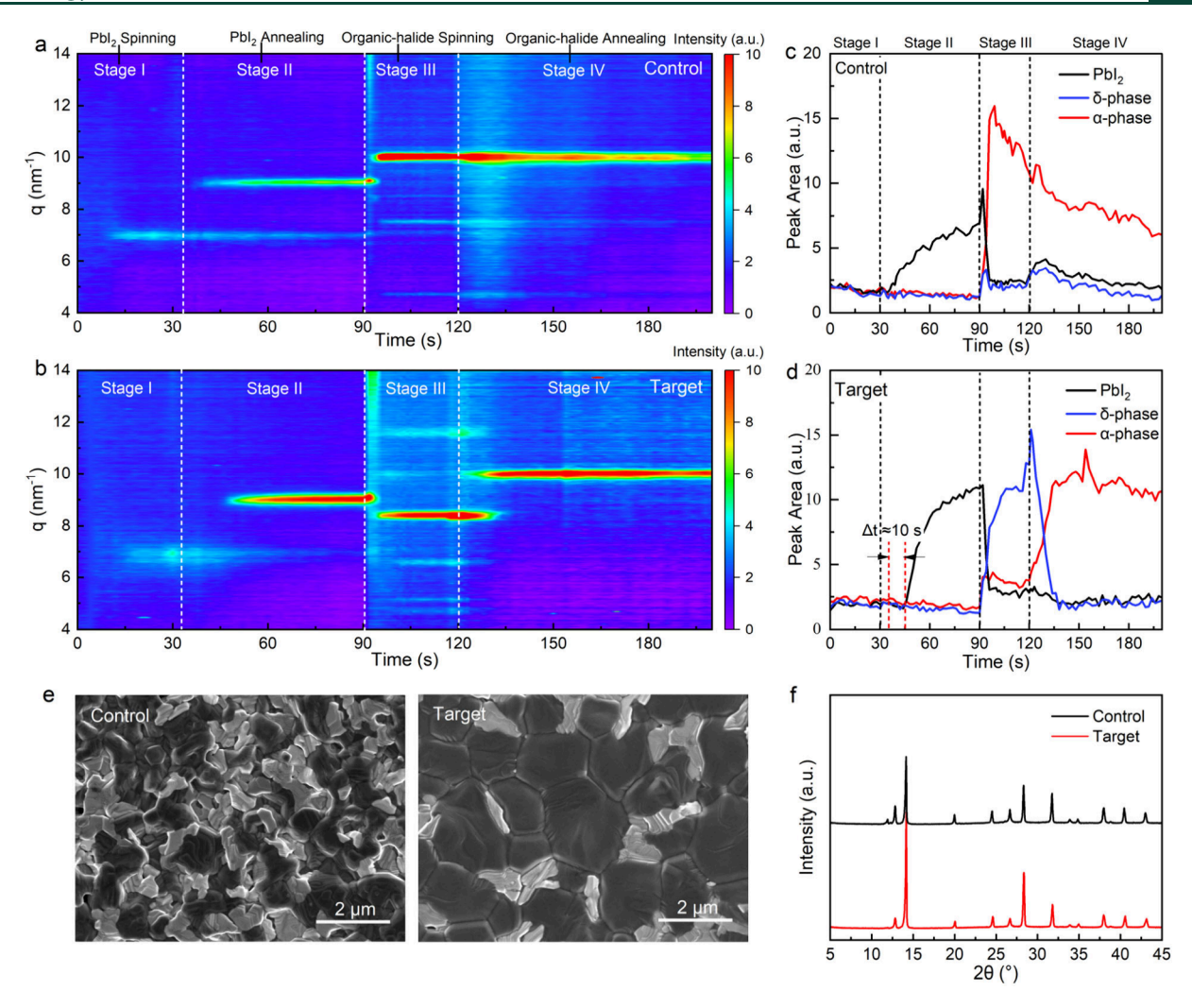


Figure 2. Characterization of the formation of the moisture-stable intermediate phase. (a, b) In situ GIWAXS spectra of control and target perovskite films deposited in ambient air. (c, d) Time-resolved integrated peak area intensities for PbI₂, the δ -phase, and the α -phase of control and target perovskite films. (e, f) SEM and XRD results of control and target perovskite films after annealing at 150 °C and 15 min.

and corresponds to the annealing process of the perovskite film.

In stage II of the control film (Figure 2a,c), the scattering halo at scattering vector **q** values near 7 nm⁻¹ is rapidly transformed into the PbI2 phase with inferior crystallinity near 9 nm⁻¹; these results from the accelerated desorption of the solvent molecules in the $PbI_2 \cdot DMSO$ complex and the continuous destruction due to moisture. The signal near $q \approx 10 \text{ nm}^{-1} \text{ of } \alpha\text{-FAPbI}_3 \text{ in stage III immediately appears after}$ the organic-halide precursor is deposited on the PbI2 film because the reaction of FAI and PbI2 is accelerated by moisture. 9,40 In addition, hydration causes a continuous decrease in the α -FAPbI $_3$ intensity, indicating severe degradation of the wet film. We conducted an aging test under humid conditions (~45% RH, ~25 $^{\circ}\text{C})$ on the wet films obtained by simple spin-coating for 10 and 20 s during a process of 30 s. After 15 min of thermal aging, the X-ray diffraction (XRD) results (Figure S4) show that the initial α -FAPbI₃ in the control wet films degrades to a state with a high ratio of δ -FAPbI₃. This heavily damaged wet film makes it difficult to produce high-quality perovskite films, even after thermal annealing in stage IV (Figure S5a).

After the incorporation of AceAc into the PbI₂ precursor, the crystallization of PbI₂ in stage II is delayed for 10 s, and the

resulting PbI₂ exhibits a more intense and more concentrated diffraction signal, indicating a stronger and more ordered crystallinity; this likely results from the incorporation of AceAc interacting with PbI2 and DMSO (Figure 2b; Figures S6 and S7 and Notes S3 and S4). In stage III, the signal of δ -FAPbI₃ rather than that of α -FAPbI₃ is generated after deposition of the organic halide precursor. δ -FAPbI₃ was the main component in the target wet film (Figure 2b,d). Even in ambient air, the intensity of the δ -FAPbI₃ signal continues to increase, indicating a negligible impact from moisture. This moisture-stable intermediate phase protects the wet film from moisture invasion and provides an undamaged state for a later purified phase transformation to attain a high-quality α -FAPbI₃. We also investigated the moisture stability of the target wet film obtained by simple spin-coating for 10 and 20 s during a complete process of 30 s. After aging for 15 min at ~45% RH and ~25 °C, the XRD results reveal that the target wet film can maintain its initial state with negligible change, showing excellent stability under humid air conditions (Figure S8). In the subsequent annealing process (stage IV), the δ -FAPbI₃-dominated wet film slowly and orderly transforms into an ideal α -FAPbI₃. ^{36,41,42} When crystallization is completed, the α -FAPbI₃ signal in the target film is more intense than that

ACS Energy Letters http://pubs.acs.org/journal/aelccp Letter

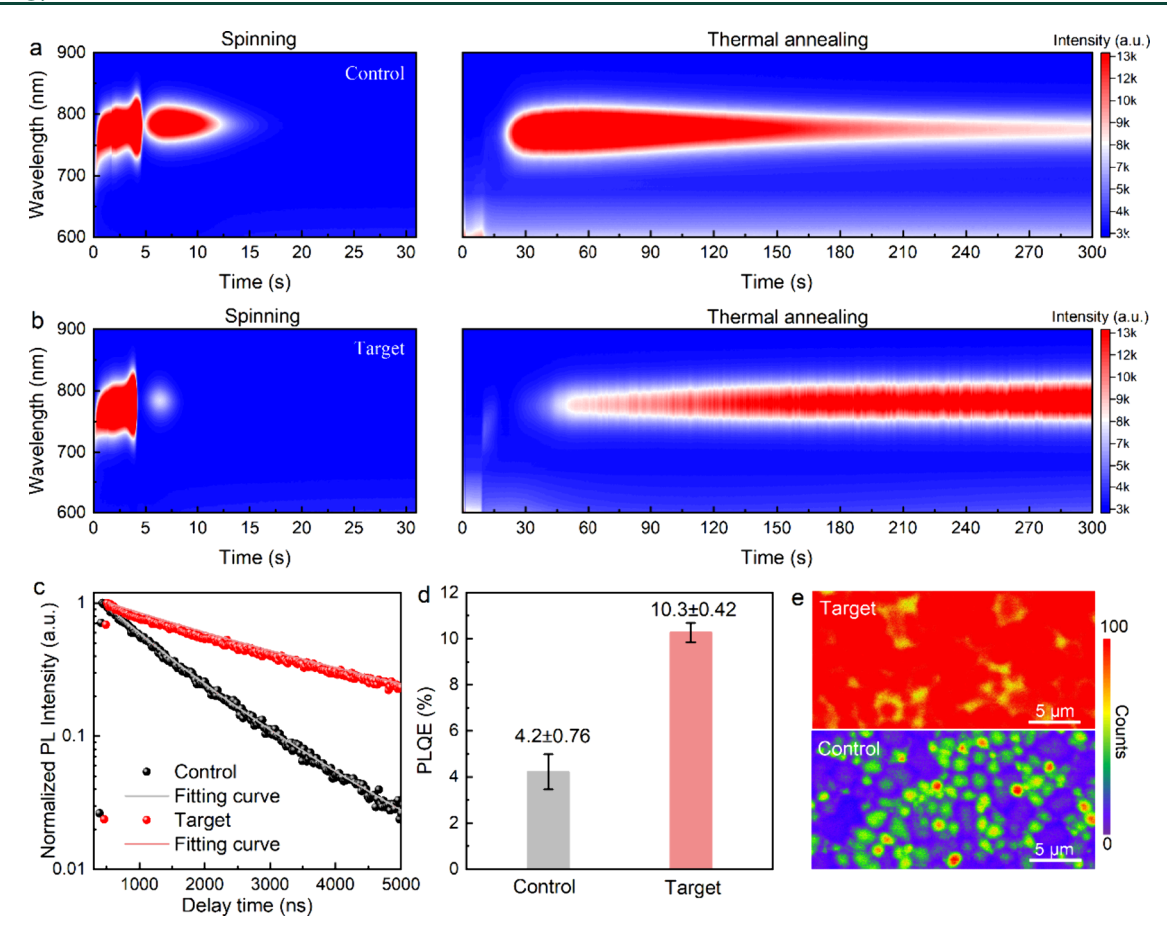


Figure 3. Influence of AceAc on the optoelectronic properties of the perovskite films. (a, b) In situ PL spectra for the control and target perovskite formation during the spin-coating process and thermal annealing process. (c) TRPL spectra of the control and target perovskite films. (d) PLQE results of the control and target perovskite films (five samples for each batch). (e) PL mapping of the target and control perovskite films.

in the control film, indicating greater crystallinity (Figure S5b,c).

Scanning electron microscopy (SEM) and XRD measurements were used to characterize the crystallization of the perovskite film. For the control film, the perovskite grains are surrounded by PbI₂ and holes (Figure 2e), which likely resulted from moisture destruction. For the target film, the perovskite grains are tightly arranged with no holes and reduced PbI₂. In addition, the perovskite grains in the target film are larger than those in the control film. The improved crystallinity of the perovskite film is also validated by the XRD results; here, the target film possesses decreased PbI2 intensity and eliminates the nonphotoactive δ -FAPbI₃, and this result is consistent with those from GIWAXS (Figure 2f). In addition, the X-ray photoelectron spectroscopy (XPS) Pb 4f spectrum of the control film includes two additional peaks located at 136.8 and 141.8 eV; these peaks are associated with Pb⁰ and are mainly caused by the moisture-induced halogen vacancies during the film formation process, and the degradation of PbI₂. Had 21,43-45 In comparison, negligible Pb⁰ peaks are observed in the Pb 4f spectrum of the target film, which also conforms to the high-quality perovskite obtained through moisture-stable δ -FAPbI₃ (Figure S9). The above results show that the constructed moisture-stable intermediate phase finely controls the crystallization kinetics of the perovskite and weakens the interference of moisture on the perovskite crystallization due to its relatively low moisture sensitivity; this enables the

successful deposition of high-quality perovskite films in ambient air.

To clarify the mechanism by which AceAc induces the formation of the moisture-stable intermediate phase, we initially studied the interaction between AceAc and PbI2. The strong interaction between PbI₂ and AceAc was confirmed by X-ray absorption fine structure (XAFS) spectroscopy. The Fourier transform spectra of the PbI₂ precursor, PbI₂ with H₂O, and PbI₂ with AceAc are shown in Figure S10. The peaks near 2.2 and 3.0 Å are associated with the Pb-O and Pb-I chemical bonds, respectively. H₂O induces numerous O²⁺ ions bound directly to Pb2+ and then weakens the Pb-I bond; this result explains the destruction of PbI2 crystallization by H2O and the collapse of the PbI₆²⁻ octahedra. From the Fourier transform spectra of the PbI₂ precursor with AceAc, Ac⁻ binds with Pb2+ through Pb-O, and the order degree of Pb-I increases. 46 The interaction between Pb2+ and Ac can also be validated by the XPS results of the final perovskite film; here, the Pb 4f peaks in the target film exhibit an evident shift to lower binding (Figure S9). The signal of Ace⁺ cations and Ac⁻ anions in time of flight-second ion mass spectroscopy (ToF-SIMS) characterization can indicate the presence of AceAc in perovskite films (Figure S11).

Then, we performed molecular dynamics (MD) simulations to gain insight into how PbI_2 in conjunction with AceAc transforms to moisture-stable δ -FAPbI₃ and then to α -FAPbI₃ after reacting with an organic halide. The simulation details

ACS Energy Letters http://pubs.acs.org/journal/aelccp Letter

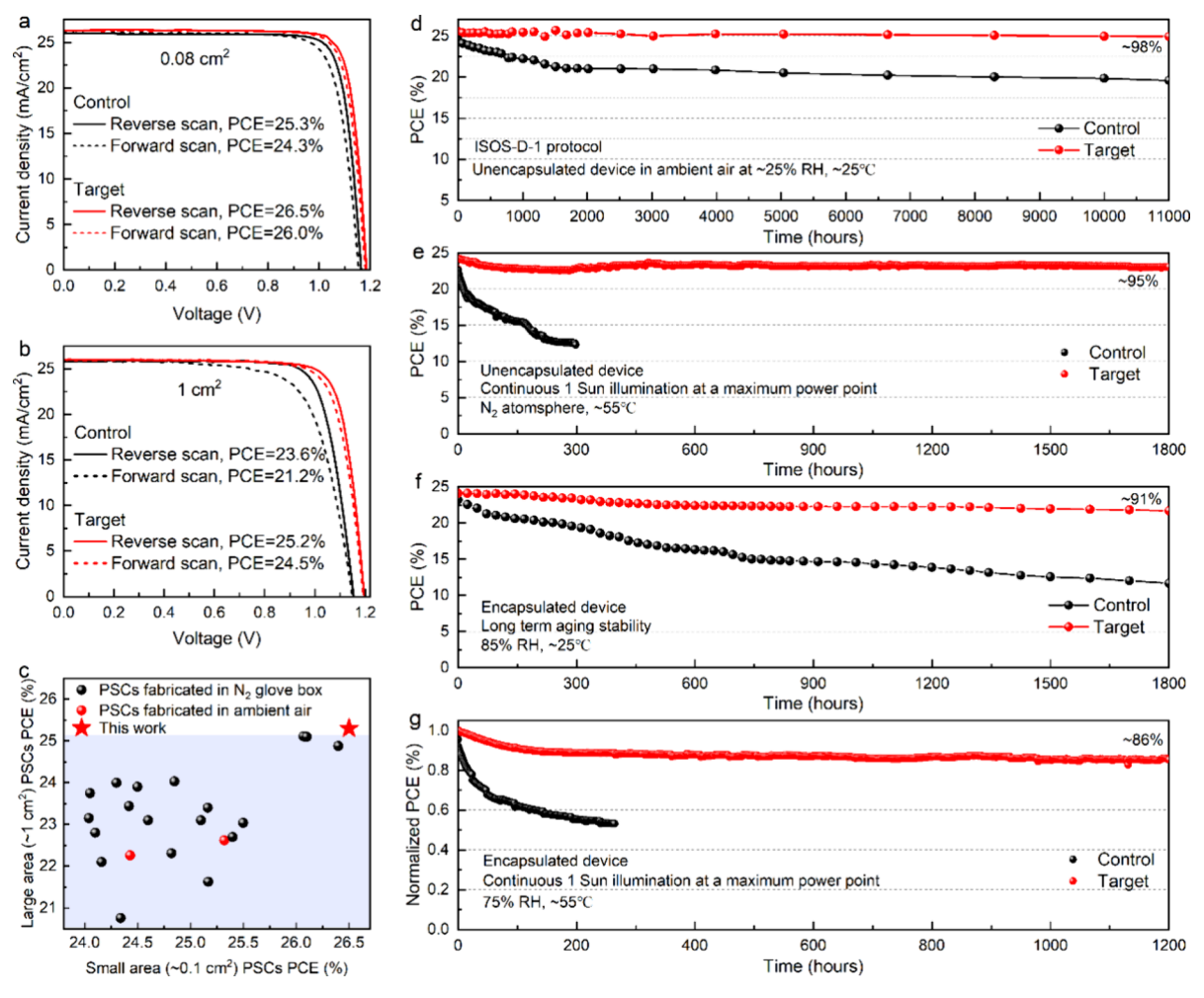


Figure 4. Photovoltaic performance of the PSCs fabricated in ambient air. (a) J-V curves of the control and target PSCs with an aperture area of 0.08 cm². (b) J-V curves of the control and target PSCs fabricated in ambient air with an aperture area of 1 cm². (c) PCE of the PSCs with simultaneously a small aperture area (\sim 0.1 cm²) and large aperture area (\sim 1 cm²). The black points represent the work of fabricating PSCs in the glovebox, the red points represent the work of fabricating PSCs in the air environment, and the red pentagram represents this work. (d) Long-term stability of the unencapsulated devices stored under ambient conditions of 25% RH and 25 °C. (e) PCE evolution of the unencapsulated devices measured at the MPP under continuous 1-sun illumination in a N₂ glovebox. (f) Long-term aging stability of the encapsulated devices stored under ambient conditions at 85% RH and 25 °C. (g) PCE evolution of the encapsulated devices measured at the MPP under continuous 1-sun illumination at 75% RH and 55 °C.

and videos are provided in the Supporting Information. As shown in Figure S12 and Movies S1 and S2, PbI₂ is twisted more violently and the average length of the Pb-I bond increases from 3.22 to 3.26 Å after the incorporation of AceAc; this shows a tendency to form δ -FAPbI₃. This potential transformation of δ -FAPbI₃ likely results from the participation of Ace+, a large cation that induces a t of 1.03 (Figure S13 and Table S3), and the strong interaction between Ac⁻ and Pb²⁺, as discussed above. We construct the δ -FAPbI₃ model systems containing AceAc, calculate the energy of the system, and find that it has a lower formation energy (Figures S14 and S15, Table S4, and Note S5);^{34,47} these results also validate those from the MD simulations and show that δ -FAPbI $_3$ can be induced by AceAc. After the formation of moisture-stable δ -FAPbI₃, we also explored how δ -FAPbI₃ transforms into final α -FAPbI₃. The MD simulations at 370 K show that δ -FAPbI₃ can be converted into α -FAPbI₃ in an orderly manner, accompanied by the movement of Ac⁻ within the lattice 48,49 (Figure S16 and Movie S3). In addition, the obtained α -FAPbI₃ shows good stability at room temperature (Movie S4).

In situ photoluminescence (PL) spectroscopy was carried out to investigate the crystallization kinetics and photoelectric performance of FAPbI₃. As shown in Figure 3a,b, when the organic halide precursor is deposited on the PbI2 film, the wet film rapidly appears as a fluorescence peak at ~770 nm in the initial stage, which is due to the rapid volatilization of solvent and the nucleation of perovskite at the liquid-gas interface, perovskite is in a dynamic process of nucleation—dissolution. So Notably, during the 30 s spin-coating process, the fluorescence peak of α-FAPbI₃ reappears again after quenching at the 5th second for the PbI₂ film without the incorporated AceAc. This occurs because the moisture can accelerate the reaction of PbI₂ with organic halide to form α -FAPbI₃. ^{38,40} However, this fluorescence peak decreases between the 7th and 15th seconds (Figure 3a and Figure S17a), indicating that constant hydration induced the decomposition of α -FAPbI₃. The decrease in the intensity of the fluorescence peak is consistent with the evident color change of the wet film, as shown in Figure S1. As the annealing process begins, the fluorescence peak of α -FAPbI₃ immediately appears due to rapid solvent

evaporation (Figure 3a and Figure S17b). However, this peak continuously decreases as the annealing process proceeds; this is likely caused by increased carrier recombination resulting from the generation of pinholes and defects (Figure 3a). The results of the in situ PL spectra demonstrate the difficulty of depositing perovskite films in ambient air, especially for the maintenance of the wet films. We employed in situ PL to monitor the crystallization process of FAPbI₃ in ambient air after constructing the moisture-stable intermediate phase. As shown in Figure 3b, Figure S17a, after the intense increase and subsequent quenching, the peak corresponding to α -FAPbI₃ at ~770 nm exhibits a negligible signal during the 30 s spincoating process, indicating that minimal α -FAPbI₃ formed in the target wet film. The lack of photoactivity of the wet film likely results from δ -FAPbI₃; this is verified to be the main component of the above GIWAXS. During the annealing process, the fluorescence peak of α -FAPbI₃ continuously increases, indicating the formation of a film with high crystallinity and excellent optoelectronic properties (Figure 3b and Figure S17b).

Time-resolved photoluminescence (TRPL) characterization was performed on the control and target films. It is noticed that the TRPL decay spectra (Figure 3c and Table S5 and Note S7) are composed of a fast decay component and a slow decay component. The τ_2 of the control perovskite film is 1.2 μ s, obviously smaller than that of the target perovskite film (4.5 μ s). The photoluminescence quantum efficiency (PLQE) was also determined. As depicted in Figure 3d, the PLQE for the control film is $4.2 \pm 0.76\%$, whereas the PLQE for the target film significantly increases, reaching 10.3 \pm 0.42%. A prolonged carrier lifetime and increased PLQE indicate fewer defect states and lower nonradiative carrier recombination within the target film. To evaluate the differences in photoelectric properties in terms of spatial uniformity, we performed confocal microscopy to characterize the control and target films (Figure 3e). The PL intensity of the target film is greater than that of the control film. In particular, the distribution of the PL intensity in the target film is more spatially uniform. The improved optoelectronic properties and spatial uniformity demonstrate that the moisture-stable intermediate phase improves the quality of perovskite films deposited in ambient air and that the AceAc in the films reduces the defect density at the grain boundaries.

We particularly characterized the moisture stability of the perovskite films. The control and target perovskite films were aged under harsh conditions at 85% RH. As the aging time increased from 0 to 48 h, the color of the control film changed from black to transparent, indicating the severe decomposition of α -FAPbI₃, which was also confirmed by the XRD results (Figure S18). In contrast, the target film maintained a stable α -phase after aging for 48 h. The improvement in the photoelectric performance and moisture stability of the target perovskite film by AceAc was beneficial for fabricating high-efficiency PSCs with excellent stability in ambient air.

We fabricated planar PSCs in ambient air $(55 \pm 5\% \text{ RH}, 25 \pm 5\,^{\circ}\text{C})$ with structures of FTO/TiO₂/perovskite (AceAc)/o-F-PEAI/Spiro-OMeTAD/Au to investigate their photovoltaic performance. After testing the PLQE and corresponding PSCs performance of perovskite films with different AceAc concentrations, we found that PSCs with 1.5 mg/mL AceAc had the best performance (Figures S19 and S20). The reverse and forward scan J-V curves of the champion control and target PSCs with an aperture area of 0.08 cm² are shown in

Figure 4a, and the corresponding photovoltaic parameters are provided in Table S6. Impressively, the target PSCs have the best PCE of 26.5%, with an open circuit voltage $(V_{\rm OC})$ of 1.19 V, a short circuit current density (J_{SC}) of 26.28 mA cm⁻², and a fill factor (FF) of 84.8% and exhibited a steady-state power output of 26.2% (Figure S21). In comparison, the control PSCs only have a maximum PCE of 25.3%, with a $V_{\rm OC}$ of 1.16 V, a J_{SC} of 25.99 mA cm⁻², and an FF of 84.0%. In addition, the target PSCs also possess a lower hysteresis in comparison to the control PSCs. The corresponding external quantum efficiency (EQE) spectra of the control and target PSCs are shown in Figure S22, yielding integrated J_{SC} values of 25.35 and 25.72 mA cm⁻², respectively. One of the best-performing target PSCs was validated by an independent accredited certification institute, the National Institute of Metrology (NIM, China); the PSC achieved a certified PCE of 25.9% (Figure S23). In addition, we fabricated a batch of control PSCs including 100 individuals, showing an average PCE of 23.9%, a J_{SC} of 25.75 mA cm⁻², a V_{OC} of 1.14 V, and an FF of 81.6%. A batch of target PSCs including 110 individuals was also fabricated, where the average PCE was 25.7% with a J_{SC} of 26.07 mA cm⁻², a $V_{\rm OC}$ of 1.18 V, and an FF of 83.7% (Figure S24). The improved PCE mainly resulted from the increase in both $V_{\rm OC}$ and FF due to the achievement of a high-quality FAPbI₃ film through a moisture-stable intermediate phase.

The photovoltaic performance of the control and target PSCs with a larger aperture area of 1 cm² validates the reliability of our study with increasing PCE and demonstrates the feasibility of our study for scalable devices. Figure 4b displays the reverse and forward scan J-V curves of the bestperforming PSCs with an aperture area of 1 cm², and the corresponding photovoltaic parameters are listed in Table S7. The target PSCs achieve a superior PCE of 25.3% (J_{SC} of 26.01 mA cm⁻², V_{OC} of 1.20 V, and an FF of 81.0%), showing an evident increase compared to that (23.6%) of the control PSCs. This result shows the great advancement of PSCs fabricated under open-air conditions. The 1 cm² PSCs were also validated by an independent accredited certification institute and achieved a certified PCE of 24.3% (Figure S25). We collected photovoltaic parameters for 90 target PSCs and 80 control PSCs (Figure S26). The average PCE of the target PCSs is 24.2%, which is superior to that (22.6%) of the control PSCs. Impressively, considering the reported PCEs of 0.08 cm² PSCs and 1 cm² PSCs, our PCEs of 26.5% for 0.08 cm² PSCs and 25.3% for 1 cm² PSCs are comparable to those of the state-of-the-art PSCs fabricated in a glovebox (Figure 4c and Table S8).

Continuous monitoring of the photovoltaic performance, including long-term storage and operating stability, was used to assess the PSCs' stability. 51,52 Figure 4d shows the long-term stability of unencapsulated devices stored in ambient air based on the ISOS-D-1 protocol.⁵³ The target device maintains ~98% of its initial PCE (25.6%, listed in Table S9), while the PCE of the control device only maintains $\sim\!80\%$ after 11000 h of storage under ambient conditions at 25% RH and 25 °C. Notably, in Figure 4e-g, we removed the organic passivation layer and replaced Spiro-OMeTAD with poly[bis(4-phenyl)-(2,4,6-trimethylphenyl)amine to better demonstrate the improvement of PSCs stability by AceAc-optimized perovskite film. The unencapsulated target device (with an initial PCE of 24.2%, as shown in Table S10) exhibits minor degradation after continuous operation for 1800 h at the maximum power point (MPP) under a N_2 atmosphere at 55 °C (Figure 4e). In

The PCE evolution of the encapsulated control and target devices stored at 85% RH and 25 °C is shown in Figure 4f. The target device can maintain \sim 91% of its initial PCE of 24.1% (Table S11) after 1800 h of storage, showing enhanced stability compared to that of the control device. We further measured the operating stability of the MPP of the encapsulated devices stored at 75% RH and 55 °C under 1 sun. As shown in Figure 4g, the PCE of the control device drops to <60% of the initial PCE (Table S12) after 200 h. In contrast, the target device retains \sim 85% of the initial PCE after 1200 h.

We constructed a moisture-stable intermediate phase in a wet film to stepwise control the perovskite crystallization by protecting the wet film from moisture invasion and then purifying the phase transformation to obtain a high-quality α -FAPbI₃ film in ambient air. This moisture-stable intermediate phase can be constructed with a variety of acetate-containing large cations, such as guanidine acetate, dimethylammonium acetate, etc., to facilitate fabrication of high-efficiency PSCs in ambient air (Figure S27). After the completion of perovskite crystallization, the residual cations bind to grain boundaries or surface sites to reduce the defect density. Consequently, we achieved PCE values of 26.5% for 0.08 cm² PSCs and 25.3% for 1 cm² PSCs. We believe that the moisture-stable crystallization pathway can provide a new insight into perovskite crystallization kinetics and facilitate the low-cost commercialization of PSC.

ASSOCIATED CONTENT

5 Supporting Information

The Supporting Information is available free of charge at https://pubs.acs.org/doi/10.1021/acsenergylett.5c02481.

Movie S1 showing behavior of PbI_2 lattice torsion after AceAe participates in the reaction between PbI_2 with the organic halide under 300 K (MP4)

Movie S2 showing the more intense twisting behavior of the PbI_2 lattice after AceAe participates in the reaction between PbI_2 with the organic halide under 300 K (MP4)

Movie S3 showing transformation of antimoisture δ -FAPbI $_3$ to α -FAPbI $_3$ under 370 K (MP4)

Experimental section including materials, device fabrication, characterization, DFT calculation, and molecular dynamics simulations; wet films photographs; AceAc chemical structure; DFT slab model system; wet films' XRD; GIWAXS, FTIR, XPS, XAFS, ToF-SIMS of PbI₂ and perovskite film; PLQE, EQE, MPPT, efficiency certification details, and statistics of photovoltaic parameters of PSCs; industrial cost calculation of PSCs; photovoltaic parameters table (PDF)

Movie S4 showing stability at 300 K of α -FAPbI₃ obtained by antimoisture δ -FAPbI₃(MP4)

AUTHOR INFORMATION

Corresponding Author

Meicheng Li — State Key Laboratory of Alternate Electrical Power System with Renewable Energy Sources, School of New Energy, North China Electric Power University, Beijing 102206, China; orcid.org/0000-0002-0731-741X; Email: mcli@ncepu.edu.cn

Authors

- Luyao Yan State Key Laboratory of Alternate Electrical Power System with Renewable Energy Sources, School of New Energy, North China Electric Power University, Beijing 102206, China
- Hao Huang State Key Laboratory of Alternate Electrical Power System with Renewable Energy Sources, School of New Energy, North China Electric Power University, Beijing 102206, China
- Peng Cui State Key Laboratory of Alternate Electrical Power System with Renewable Energy Sources, School of New Energy, North China Electric Power University, Beijing 102206, China
- Yingying Yang State Key Laboratory of Alternate Electrical Power System with Renewable Energy Sources, School of New Energy, North China Electric Power University, Beijing 102206, China
- Zhenhuang Su Shanghai Synchrotron Radiation Facility, Shanghai Advanced Research Institute, Chinese Academy of Sciences, Shanghai 201204, China; ⊙ orcid.org/0000-0003-0026-2601
- Yi Lu State Key Laboratory of Alternate Electrical Power System with Renewable Energy Sources, School of New Energy, North China Electric Power University, Beijing 102206, China
- Min Wang State Key Laboratory of Alternate Electrical Power System with Renewable Energy Sources, School of New Energy, North China Electric Power University, Beijing 102206, China
- Zhineng Lan State Key Laboratory of Alternate Electrical Power System with Renewable Energy Sources, School of New Energy, North China Electric Power University, Beijing 102206, China
- Shujie Qu State Key Laboratory of Alternate Electrical Power System with Renewable Energy Sources, School of New Energy, North China Electric Power University, Beijing 102206, China
- Benyu Liu State Key Laboratory of Alternate Electrical Power System with Renewable Energy Sources, School of New Energy, North China Electric Power University, Beijing 102206, China
- Changxu Sun State Key Laboratory of Alternate Electrical Power System with Renewable Energy Sources, School of New Energy, North China Electric Power University, Beijing 102206, China
- Liang Li State Key Laboratory of Alternate Electrical Power System with Renewable Energy Sources, School of New Energy, North China Electric Power University, Beijing 102206, China
- Shuxian Du State Key Laboratory of Alternate Electrical Power System with Renewable Energy Sources, School of New Energy, North China Electric Power University, Beijing 102206, China
- Fu Yang State Key Laboratory of Alternate Electrical Power System with Renewable Energy Sources, School of New Energy, North China Electric Power University, Beijing 102206, China
- Xingyu Gao Shanghai Synchrotron Radiation Facility, Shanghai Advanced Research Institute, Chinese Academy of Sciences, Shanghai 201204, China

Complete contact information is available at: https://pubs.acs.org/10.1021/acsenergylett.5c02481

Author Contributions

§L.Y., H.H., P.C., and Y.Y. contributed equally to this work. M.L., L.Y., H.H., and P.C. conceived the idea. M.L., H.H., and P.C. guided the work as supervisors. L.Y. did experimental designs, device fabrication, and data analysis. Y.Y., Z.S., Y.L., and M.W. were involved in device fabrication and conducted part of the characterizations. Z.L, P.C., L.L., and X.G. assisted with in situ GIWAXS and PL spectra testing. B.L. provided support for the calculation of production lines costs. L.Y., H.H., and P.C. drafted the initial version of the manuscript. C.S., S.D., and F.Y. contributed to the manuscript revision and language polishing. All authors participated in discussing the results and contributed to revising the manuscript.

Notes

The authors declare no competing financial interest.

ACKNOWLEDGMENTS

We sincerely thank the Beijing Synchrotron Radiation Facility (BSRF) for the facility support of the 1W1B beamline, and the Shanghai Synchrotron Radiation Facility (SSRF) for the facility support of the BL14B beamline. This work is supported partially by the Beijing Natural Science Foundation (Z240024), National Natural Science Foundation of China (Grant Nos. 52232008, 52402254, 52102245, and 22409061), Beijing Nova Program (20220484016), Young Elite Scientists Sponsorship Program by CAST (2022QNRC001), Huaneng Group Headquarters Science and Technology Project (HNKJ20-H88), the Fundamental Research Funds for the Central Universities (2023MS042, 2024MS036, 2023MS047, 2024MS039, 2024JC005, and 2025MS038), the Postdoctoral Fellowship Program of CPSF under Grant No. GZB20250045, and the NCEPU "Double First-Class" Program.

REFERENCES

- (1) Li, Q.; Zheng, Y.; Wang, H.; Liu, X.; Lin, M.; Sui, X.; Leng, X.; Liu, D.; Wei, Z.; Song, M.; et al. Graphene-polymer reinforcement of perovskite lattices for durable solar cells. *Science* **2025**, 387 (6738), 1069–1077.
- (2) Ma, C.; Eickemeyer, F. T.; Lee, S.-H.; Kang, D.-H.; Kwon, S. J.; Grätzel, M.; Park, N.-G. Unveiling facet-dependent degradation and facet engineering for stable perovskite solar cells. *Science* **2023**, *379* (6628), 173–178.
- (3) Zhou, S.; Fu, S.; Wang, C.; Meng, W.; Zhou, J.; Zou, Y.; Lin, Q.; Huang, L.; Zhang, W.; Zeng, G.; et al. Aspartate all-in-one doping strategy enables efficient all-perovskite tandems. *Nature* **2023**, *624* (7990), 69–73.
- (4) Nie, R.; Zhang, P.; Gao, J.; Wang, C.; Chu, W.; Li, L.; Wang, K.; Qian, D.; Lin, F.; Xia, X.; et al. Enhanced coordination interaction with multi-site binding ligands for efficient and stable perovskite solar cells. *Nat. Commun.* **2025**, *16* (1), 6438.
- (5) Zhang, Y.; Yang, T.; Lee, S.-U.; Liu, S.; Zhao, K.; Park, N.-G. Stabilizing α -Phase FAPbI $_3$ Perovskite Induced by an Ordered Solvated Quasi-Crystalline PbI $_2$. ACS Energy Lett. **2024**, 9 (1), 159–167.
- (6) Shi, P.; Ding, Y.; Ding, B.; Xing, Q.; Kodalle, T.; Sutter-Fella, C. M.; Yavuz, I.; Yao, C.; Fan, W.; Xu, J.; et al. Oriented nucleation in formamidinium perovskite for photovoltaics. *Nature* **2023**, *620* (7973), 323–327.
- (7) Sidhik, S.; Metcalf, I.; Li, W.; Kodalle, T.; Dolan, C. J.; Khalili, M.; Hou, J.; Mandani, F.; Torma, A.; Zhang, H.; et al. Two-dimensional perovskite templates for durable, efficient formamidinium perovskite solar cells. *Science* **2024**, 384 (6701), 1227–1235.
- (8) Meng, H.; Mao, K.; Cai, F.; Zhang, K.; Yuan, S.; Li, T.; Cao, F.; Su, Z.; Zhu, Z.; Feng, X.; et al. Inhibition of halide oxidation and deprotonation of organic cations with dimethylammonium formate

- for air-processed p-i-n perovskite solar cells. Nat. Energy 2024, 9 (5), 536-547.
- (9) Zou, Y.; Yu, W.; Guo, H.; Li, Q.; Li, X.; Li, L.; Liu, Y.; Wang, H.; Tang, Z.; Yang, S.; et al. A crystal capping layer for formation of blackphase FAPbI₃ perovskite in humid air. *Science* **2024**, 385 (6705), 161–167.
- (10) Yang, G.; Gu, H.; Yin, J.; Fei, C.; Shi, Z.; Shi, X.; Ying, X.; Huang, J. Reductive cation for scalable wide-bandgap perovskite solar cells in ambient air. *Nat. Sustainability* **2025**, 8 (4), 456–463.
- (11) Il Jake Choi, J.; Ono, L. K.; Cho, H.; Kim, K.-J.; Kang, H.-B.; Qi, Y.; Park, J. Y. Pathways of Water-Induced Lead-Halide Perovskite Surface Degradation: Insights from In Situ Atomic-Scale Analysis. *ACS Nano* **2023**, *17* (24), 25679–25688.
- (12) Kim, S.-W.; Moon, S. J.; Kim, S.-H.; Yoo, J. J.; Kim, D.; Kim, B.-S.; Jeon, N. J. Reducing Humidity Dependency of Ambient-Air-Processed Wide-Bandgap Inverted Perovskite Solar Cells. *ACS Energy Lett.* **2023**, 8 (11), 4777–4781.
- (13) Gao, H.; Xiao, K.; Lin, R.; Zhao, S.; Wang, W.; Dayneko, S.; Duan, C.; Ji, C.; Sun, H.; Bui, A. D.; et al. Homogeneous crystallization and buried interface passivation for perovskite tandem solar modules. *Science* **2024**, 383 (6685), 855–859.
- (14) Dai, X.; Chen, S.; Jiao, H.; Zhao, L.; Wang, K.; Ni, Z.; Yu, Z.; Chen, B.; Gao, Y.; Huang, J. Efficient monolithic all-perovskite tandem solar modules with small cell-to-module derate. *Nat. Energy* **2022**, *7* (10), 923–931.
- (15) Zuo, C.; Ding, L. Drop-Casting to Make Efficient Perovskite Solar Cells under High Humidity. *Angew. Chem., Int. Ed.* **2021**, *60* (20), 11242–11246.
- (16) Zheng, X.; Kong, W.; Wen, J.; Hong, J.; Luo, H.; Xia, R.; Huang, Z.; Luo, X.; Liu, Z.; Li, H.; et al. Solvent engineering for scalable fabrication of perovskite/silicon tandem solar cells in air. *Nat. Commun.* **2024**, *15* (1), 4907.
- (17) Duan, C.; Gao, H.; Xiao, K.; Yeddu, V.; Wang, B.; Lin, R.; Sun, H.; Wu, P.; Ahmed, Y.; Bui, A. D.; et al. Scalable fabrication of wide-bandgap perovskites using green solvents for tandem solar cells. *Nat. Energy* **2025**, *10* (3), 318–328.
- (18) Wu, G.; Wang, J.; Fang, X.; Xu, J.; Xia, X.; Zhao, J.; Zheng, L.; Zhang, M.; Chen, Z.; Chen, H.; et al. Two-Step Inverted Perovskite Solar Cells with > 25% Efficiency Fabricated in Ambient Air. *Adv. Energy Mater.* **2025**, *15* (27), 2500830.
- (19) Zhu, X.; Yu, D.; Zhou, X.; Wang, N.; Liu, H.; Liang, Z.; Wu, C.; Wang, K.; Jin, D.; Liu, S.; et al. Interfacial molecular anchor for ambient all-bladed perovskite solar modules. *Joule* **2025**, *9* (5), 101919.
- (20) Yuan, L.; Chen, X.; Guo, X.; Huang, S.; Wu, X.; Shen, Y.; Gu, H.; Chen, Y.; Zeng, G.; Egelhaaf, H.-J.; et al. Volatile Perovskite Precursor Ink Enables Window Printing of Phase-Pure FAPbI₃ Perovskite Solar Cells and Modules in Ambient Atmosphere. *Angew. Chem., Int. Ed.* **2024**, 63 (7), No. e202316954.
- (21) Hu, X.; Zhao, C.; Liu, Y.; Li, J.-A.; Wang, L.; Tang, X.; Dou, Y.; Shi, X.; Liu, T.; Luo, S.; et al. Blade-Coated Perovskite-Organic Tandem Solar Cells in Ambient Conditions. *Adv. Funct. Mater.* **2025**, No. e12093.
- (22) Luo, H.; Han, X.; Yang, B.; Ou, W.; Suo, J.; Sun, H.; Zheng, X.; Hong, J.; Chu, Z.; Zhao, L.; et al. Damp-Stable Perovskite/Silicon Tandem Solar Cells with Internal Encapsulating Sulfonium-Based Molecules. ACS Energy Lett. 2025, 10 (7), 3325–3334.
- (23) Liu, T.; Ren, Z.; Liu, Y.; Zhang, Y.; Liang, J.; Cheng, F.; Li, Y.; Shi, X.; Dou, Y.; Hu, X.; et al. Efficient perovskite solar modules enabled by a UV-stable and high-conductivity hole transport material. *Sci. Adv.* **2025**, *11* (22), No. eadu3493.
- (24) Lv, L.; Zuo, C.; Zhang, L.; Xiao, Z.; Bao, Q.; Yi, C.; Chang, J.; Yan, K.; Ding, Y.; Wu, C.; et al. Efficient Perovskite Solar Cells Made by Using a Vapor-Assisted Hot Crystallization Method in Air. *Small* **2025**, No. e06937.
- (25) Hui, W.; Chao, L.; Lu, H.; Xia, F.; Wei, Q.; Su, Z.; Niu, T.; Tao, L.; Du, B.; Li, D.; et al. Stabilizing black-phase formamidinium perovskite formation at room temperature and high humidity. *Science* **2021**, *371* (6536), 1359–1364.

- (26) Yang, Y.; Huang, H.; Yan, L.; Cui, P.; Lan, Z.; Sun, C.; Du, S.; Wang, X.; Yao, C.; Qu, S.; et al. Compatible Soft-Templated Deposition and Surface Molecular Bridge Construction of SnO₂ Enable Air-Fabricated Perovskite Solar Cells with Efficiency Exceeding 25.7%. *Adv. Energy Mater.* **2024**, *14*, 2400416.
- (27) Yan, L.; Huang, H.; Cui, P.; Du, S.; Lan, Z.; Yang, Y.; Qu, S.; Wang, X.; Zhang, Q.; Liu, B.; et al. Fabrication of perovskite solar cells in ambient air by blocking perovskite hydration with guanabenz acetate salt. *Nat. Energy* **2023**, *8* (10), 1158–1167.
- (28) Čulík, P.; Brooks, K.; Momblona, C.; Adams, M.; Kinge, S.; Maréchal, F.; Dyson, P. J.; Nazeeruddin, M. K. Design and Cost Analysis of 100 MW Perovskite Solar Panel Manufacturing Process in Different Locations. *ACS Energy Lett.* **2022**, *7* (9), 3039–3044.
- (29) Cai, M.; Wu, Y.; Chen, H.; Yang, X.; Qiang, Y.; Han, L. Cost-Performance Analysis of Perovskite Solar Modules. *Adv. Sci.* **2017**, *4* (1), 1600269.
- (30) Zafoschnig, L. A.; Nold, S.; Goldschmidt, J. C. The Race for Lowest Costs of Electricity Production: Techno-Economic Analysis of Silicon, Perovskite and Tandem Solar Cells. *IEEE Journal of Photovoltaics* **2020**, *10* (6), 1632–1641.
- (31) Song, Z.; McElvany, C. L.; Phillips, A. B.; Celik, I.; Krantz, P. W.; Watthage, S. C.; Liyanage, G. K.; Apul, D.; Heben, M. J. A technoeconomic analysis of perovskite solar module manufacturing with low-cost materials and techniques. *Energy Environ. Sci.* **2017**, *10* (6), 1297–1305.
- (32) Li, G.; Su, Z.; Canil, L.; Hughes, D.; Aldamasy, M. H.; Dagar, J.; Trofimov, S.; Wang, L.; Zuo, W.; Jerónimo-Rendon, J. J.; et al. Highly efficient p-i-n perovskite solar cells that endure temperature variations. *Science* **2023**, 379 (6630), 399–403.
- (33) Fu, C.; Gu, Z.; Tang, Y.; Xiao, Q.; Zhang, S.; Zhang, Y.; Song, Y. From Structural Design to Functional Construction: Amine Molecules in High-Performance Formamidinium-Based Perovskite Solar Cells. *Angew. Chem., Int. Ed.* **2022**, *61* (19), No. e202117067.
- (34) Kim, M.; Kim, G.-H.; Lee, T. K.; Choi, I. W.; Choi, H. W.; Jo, Y.; Yoon, Y. J.; Kim, J. W.; Lee, J.; Huh, D.; et al. Methylammonium Chloride Induces Intermediate Phase Stabilization for Efficient Perovskite Solar Cells. *Joule* **2019**, 3 (9), 2179–2192.
- (35) Jeong, J.; Kim, M.; Seo, J.; Lu, H.; Ahlawat, P.; Mishra, A.; Yang, Y.; Hope, M. A.; Eickemeyer, F. T.; Kim, M.; et al. Pseudohalide anion engineering for α -FAPbI₃ perovskite solar cells. *Nature* **2021**, 592 (7854), 381–385.
- (36) Lu, H.; Liu, Y.; Ahlawat, P.; Mishra, A.; Tress, W. R.; Eickemeyer, F. T.; Yang, Y.; Fu, F.; Wang, Z.; Avalos, C. E.; et al. Vapor-assisted deposition of highly efficient, stable black-phase FAPbI₃ perovskite solar cells. *Science* **2020**, *370* (6512), No. eabb8985.
- (37) Zhang, K.; Wang, Z.; Wang, G.; Wang, J.; Li, Y.; Qian, W.; Zheng, S.; Xiao, S.; Yang, S. A prenucleation strategy for ambient fabrication of perovskite solar cells with high device performance uniformity. *Nat. Commun.* **2020**, *11* (1), 1006.
- (38) Guo, R.; Xiong, Q.; Ulatowski, A.; Li, S.; Ding, Z.; Xiao, T.; Liang, S.; Heger, J. E.; Guan, T.; Jiang, X.; et al. Trace Water in Lead Iodide Affecting Perovskite Crystal Nucleation Limits the Performance of Perovskite Solar Cells. *Adv. Mater.* **2024**, *36* (7), 2310237.
- (39) Lin, D.; Fang, J.; Yang, X.; Wang, X.; Li, S.; Wang, D.; Xie, G.; Li, H.; Wang, X.; Qiu, L. Modulating the Distribution of Formamidinium Iodide by Ultrahigh Humidity Treatment Strategy for High-Quality Sequential Vapor Deposited Perovskite. *Small* **2024**, 20 (12), 2307960.
- (40) Liu, K.; Luo, Y.; Jin, Y.; Liu, T.; Liang, Y.; Yang, L.; Song, P.; Liu, Z.; Tian, C.; Xie, L.; et al. Moisture-triggered fast crystallization enables efficient and stable perovskite solar cells. *Nat. Commun.* **2022**, 13 (1), 4891.
- (41) Du, X.; Zhang, J.; Su, H.; Guo, X.; Hu, Y.; Liu, D.; Yuan, N.; Ding, J.; Gao, L.; Liu, S. Synergistic Crystallization and Passivation by a Single Molecular Additive for High-Performance Perovskite Solar Cells. *Adv. Mater.* **2022**, *34* (33), 2204098.
- (42) Pan, T.; Zhou, W.; Wei, Q.; Peng, Z.; Wang, H.; Jiang, X.; Zang, Z.; Li, H.; Yu, D.; Zhou, Q.; et al. Surface-Energy-Regulated

- Growth of α -Phase Cs_{0.03}FA_{0.97}PbI₃ for Highly Efficient and Stable Inverted Perovskite Solar Cells. *Adv. Mater.* **2023**, 35 (15), 2208522. (43) Tang, W.; Liu, T.; Zhang, M.; Yuan, F.; Zhou, K.; Lai, R.; Lian, Y.; Xing, S.; Xiong, W.; Zhang, M.; et al. The roles of metal oxidation states in perovskite semiconductors. *Matter* **2023**, 6 (11), 3782–3802.
- (44) Chen, T.; Yang, Y.; Zhu, C.; Lin, W.; Dai, Q.; Guo, X. Revealing the stability origins of 596 days-humidity-stable semitransparent perovskite solar cells. *J. Energy Chem.* **2024**, 94, 208–216. (45) Liu, L.; Ma, Y.; Wang, Y.; Ma, Q.; Wang, Z.; Yang, Z.; Wan, M.; Mahmoudi, T.; Hahn, Y.-B.; Mai, Y. Hole-Transport Management Enables 23%-Efficient and Stable Inverted Perovskite Solar Cells with 84% Fill Factor. *Nano-Micro Lett.* **2023**, 15 (1), 117.
- (46) Min, H.; Lee, D. Y.; Kim, J.; Kim, G.; Lee, K. S.; Kim, J.; Paik, M. J.; Kim, Y. K.; Kim, K. S.; Kim, M. G.; et al. Perovskite solar cells with atomically coherent interlayers on SnO_2 electrodes. *Nature* **2021**, 598 (7881), 444–450.
- (47) Ye, F.; Ma, J.; Chen, C.; Wang, H.; Xu, Y.; Zhang, S.; Wang, T.; Tao, C.; Fang, G. Roles of MACl in Sequentially Deposited Bromine-Free Perovskite Absorbers for Efficient Solar Cells. *Adv. Mater.* **2021**, 33 (3), 2007126.
- (48) Lee, D.-K.; Jeong, D.-N.; Ahn, T. K.; Park, N.-G. Precursor Engineering for a Large-Area Perovskite Solar Cell with > 19% Efficiency. ACS Energy Lett. 2019, 4 (10), 2393–2401.
- (49) Chen, C.-H.; Lou, Y.-H.; Wang, K.-L.; Su, Z.-H.; Dong, C.; Chen, J.; Shi, Y.-R.; Gao, X.-Y.; Wang, Z.-K. Ternary Two-Step Sequential Deposition Induced Perovskite Orientational Crystallization for High-Performance Photovoltaic Devices. *Adv. Energy Mater.* **2021**, *11* (30), 2101538.
- (50) Wang, S.; Yang, T.; Yang, Y.; Du, Y.; Huang, W.; Cheng, L.; Li, H.; Wang, P.; Wang, Y.; Zhang, Y.; et al. In Situ Self-Elimination of Defects via Controlled Perovskite Crystallization Dynamics for High-Performance Solar Cells. *Adv. Mater.* **2023**, 35 (42), 2305314.
- (51) Li, X.; Fu, S.; Liu, S.; Wu, Y.; Zhang, W.; Song, W.; Fang, J. Suppressing the ions-induced degradation for operationally stable perovskite solar cells. *Nano Energy* **2019**, *64*, 103962.
- (52) Li, X.; Zhang, W.; Guo, X.; Lu, C.; Wei, J.; Fang, J. Constructing heterojunctions by surface sulfidation for efficient inverted perovskite solar cells. *Science* **2022**, *375* (6579), 434–437.
- (53) Khenkin, M. V.; Katz, E. A.; Abate, A.; Bardizza, G.; Berry, J. J.; Brabec, C.; Brunetti, F.; Bulović, V.; Burlingame, Q.; Di Carlo, A.; et al. Consensus statement for stability assessment and reporting for perovskite photovoltaics based on ISOS procedures. *Nat. Energy* **2020**, *5* (1), 35–49.